



Photocatalytic degradation of Indigo Carmine using aluminum-doped titanium dioxide/zinc ferrite nanocomposite under visible light

Hossein Abdolmohammad-Zadeh¹ · Zeynab Talleb² · Mohammad Khalili¹

Received: 17 January 2022 / Accepted: 25 September 2022 / Published online: 6 October 2022
© Iranian Chemical Society 2022

Abstract

In this study, a novel visible light-active photocatalyst named aluminum-doped titanium dioxide/zinc ferrite (Al-TiO₂/ZnFe₂O₄) nanocomposite was successfully synthesized by sol-gel and mechano-chemical routes. The structural properties of the fabricated photocatalyst were characterized using X-ray diffraction, scanning electron microscopy, energy-dispersive X-ray spectroscopy, diffuse reflectance UV-vis spectroscopy, and Fourier transform infrared spectroscopy. The capability of the prepared photocatalyst was evaluated for the photodegradation of Indigo Carmine dye. It was observed that the Al-TiO₂/ZnFe₂O₄ nanocomposite containing 0.5%wt Al and 5.0%wt ZnFe₂O₄ could completely degrade Indigo Carmine under visible light irradiation. Numerous factors affecting the photocatalytic process efficiency, such as pH, amount of the nano-photocatalyst, and concentration of the dye, were investigated and optimized. Total organic carbon measurement was carried out to determine the rate of Indigo Carmine dye mineralization in the photodegradation process. The nanocomposite showed good stability for three replication of the photocatalytic reaction. The kinetics of the reaction was studied, and based on the obtained results, the photocatalytic degradation of Indigo Carmine follows pseudo-first-order degradation kinetics. Trapping experiments using various scavengers indicated that the holes (h⁺) and superoxide radical (O₂⁻) were the main reactive species in the photodegradation process of Indigo Carmine dye.

Keywords Photodegradation · Nano-photocatalyst · Al-doped titanium dioxide/zinc ferrite nanocomposite · Indigo Carmine · Visible light

Introduction

Indigo Carmine (IC) is widely used as a colorant in different industries such as food and beverage, printing, paper, cosmetics, carpet, leather, medical products and textiles [1]. Although it is also used as a diagnostic agent for kidney function test and tumor imaging [2], its major application is in the textile sector for dyeing. Unfortunately, about 20% of the unspent dye is directly released into the environment in the form of wastewater. The discharged dye poses a serious threat to the environment as the dye is toxic, mutagenic and potentially carcinogenic and causes permanent corneal

damage, eyes and skin irritation, vomiting and diarrhea [3–7]. Thus, various methods such as adsorption, chemical oxidation, electro-Fenton and photoelectro-Fenton oxidation, direct UV-C treatment and hybrid photo-electrocatalytic/photoelectron-Fenton oxidation [8–11] have been developed to remove IC dye from the textile industry effluents. However, these methods lead to incomplete degradation of the pollutant, and they only cause the pollution to be transferred from one phase to the other phase. Moreover, the requirement of refinements and high cost are other drawbacks of these methods [12, 13].

To deal with the above-mentioned problems, advanced oxidation processes (AOPs) have been developed [14]. Among the AOPs, semiconductor photocatalysis has the potential for total degradation of organic pollutants [15–18]. In a photocatalysis process, to support or accelerate a chemical reaction, light and catalyst are simultaneously used [19]. In heterogeneous photocatalysis, photon activation of a semiconductor plays a significant role. By photo-irradiation of a semiconducting material (catalyst)

✉ Hossein Abdolmohammad-Zadeh
h.abdol@azaruniv.ac.ir; h_abdol@yahoo.com

¹ Department of Chemistry, Faculty of Sciences, Azarbaijan Shahid Madani University, 35 Km Tabriz-Maragheh Road, P.O. Box 53714-161, Tabriz 5375171379, Iran

² Research and Development Department, Zahravi Pharmaceutical Company, Tabriz, Iran

with lights comprising of energies higher than its bandgap, electron–hole pairs are produced so that photoexcited electrons at the conduction band act as reduction sites, and the holes at the valence band act as oxidizing centers, leading to a photocatalytic reaction [20].

Photocatalysis is generally known with titanium dioxide (TiO_2) since it is the classic semiconductor that has been historically used in this field. The TiO_2 nanoparticles have excellent photocatalytic properties, but due to the wide bandgap of these nanoparticles, their absorption is limited to the ultraviolet region. Since sunlight contains just 5% of ultraviolet light, titanium dioxide nanoparticles do not have the desired photocatalytic activity in the presence of sunlight [21, 22]. Consequently, the development of visible-light-responsive titanium dioxide-based photocatalysts is essential for environmental applications. To extend the absorption wavelength of titanium dioxide from the ultraviolet to the visible light region, numerous approaches such as doping and surface modification have been introduced. One strategy to reduce the bandgap is doping of TiO_2 with other narrow bandgap semiconductors such as ZnS and CdS . In this case, new energy levels are introduced between the valence and conduction bands of TiO_2 , promoting the separation of the generated electron–hole pairs [23]. On the other hand, to further improve the photocatalytic process efficiency, mixing TiO_2 with metal and noble metals such as Ag , Fe , Cr , Cu , Au , and Pt has been considered as a promising strategy. These can act as a sink for photo-induced charge carriers, promoting interfacial charge-transfer processes [24–29].

In the present study, a novel and reusable photocatalyst named aluminum-doped titanium dioxide/zinc ferrite ($\text{Al-TiO}_2/\text{ZnFe}_2\text{O}_4$) nanocomposite with an excellent photoactivity under visible light irradiation toward Indigo Carmine was synthesized. After characterization using several methods, the influence of numerous factors on the photocatalytic degradation efficiency of $\text{Al-TiO}_2/\text{ZnFe}_2\text{O}_4$ nanocomposite was investigated by a UV–vis spectrophotometer, and a possible mechanism of the photocatalytic degradation is also proposed.

To the best of our knowledge, so far, no attempt has been made to prepare highly effective and reusable photocatalyst based on $\text{Al-TiO}_2/\text{ZnFe}_2\text{O}_4$. Aluminum ion could be introduced to titanium dioxide as a substitute because of its close ionic radius to titanium. Although the spinel ZnFe_2O_4 semiconductor can absorb the visible light due to its narrow bandgap, due to the small potential of the valence band and as well as the poor photoelectric properties in light transformation and the recombination of the electron–hole, it cannot be used alone and directly in the photodegradation of organic pollutants [30–32]. Accordingly, the combination

of Al-doped TiO_2 with ZnFe_2O_4 nanoparticles can result in a novel photocatalyst with improved properties.

Experimental

Reagents and standards

All materials used in this study were of analytical reagent grade. Titanium dioxide p25 Degussa, aluminum nitrate nonahydrate, zinc nitrate hexahydrate, ferric nitrate nonahydrate, Indigo Carmine, methanol, ethanol, sodium hydroxide, sodium chloride, ammonia solution 25%, hydrochloric acid 37%, and citric acid were purchased from Merck. Deionized water was used to make all the solutions. To prepare a stock solution of Indigo Carmine (1000 mg L^{-1}), 50 mg of Indigo Carmine was dissolved in a 50.0-mL volumetric flask and made up with deionized water. Hydrochloric acid, sodium hydroxide, and sodium chloride solutions with desired concentrations were prepared with the stepwise dilution of the stock solutions.

Preparation of $\text{Al-TiO}_2/\text{ZnFe}_2\text{O}_4$

The magnetic ZnFe_2O_4 nanoparticles were prepared using a sol–gel process. Briefly, 4.04 g of $\text{Fe}(\text{NO}_3)_3 \cdot 9\text{H}_2\text{O}$ and 2.97 g of $\text{Zn}(\text{NO}_3)_2 \cdot 6\text{H}_2\text{O}$ were mixed and stirred in 80 mL deionized water for 30 min to form a well-mixed solution. Then, 2 g citric acid was added to the stirring solution. To adjust the solution's pH to about 7, ammonia solution was added dropwise to the solution. After heating the mixture at $80 \text{ }^\circ\text{C}$ for 4 h, a brown gel was obtained. The gel was dried at $70 \text{ }^\circ\text{C}$ for 12 h in an oven to form a crystalline structure of ZnFe_2O_4 . Thereafter, the powder was calcinated at $600 \text{ }^\circ\text{C}$ for 4 h [33].

To prepare aluminum-doped titanium dioxide with different mass percentages of Al (0.2 wt%, 0.5 wt%, 1wt%, and 2wt%), in the first step, 0.25 g of titanium dioxide p25 nanoparticles was dispersed in 25 mL methanol, respectively, and 0.0069, 0.017, 0.034, and 0.069 g of $\text{Al}(\text{NO}_3)_3 \cdot 9\text{H}_2\text{O}$ were added to the suspension. The solution was stirred continuously at ambient temperature overnight. Al-TiO_2 nanoparticles were obtained by drying at $70 \text{ }^\circ\text{C}$ and sintering at $600 \text{ }^\circ\text{C}$ for 4 h [34, 35].

$\text{Al-TiO}_2/\text{ZnFe}_2\text{O}_4$ nanocomposites with different percentages of zinc ferrite (2 wt%, 5 wt%, 10 wt%, and 30 wt%) were prepared with a simple mechano-chemical method. For this, 0.5 g of Al-TiO_2 nanoparticles and, respectively, 0.01, 0.025, 0.05, and 0.15 g of as-synthesized ZnFe_2O_4 nanoparticles were dispersed in 5 mL ethanol, stirred for 6 h, and dried at $75 \text{ }^\circ\text{C}$ overnight [30].

Characterization of Al-TiO₂/ZnFe₂O₄

The Fourier transform infrared spectroscopy (FT-IR, BRUKER) was used to identify the chemical nature and functional groups. X-ray diffractometer (XRD, D8 ADVANCE) manufactured by BRUKER AXS was employed for crystalline phase structure characterization of the synthesized samples. The surface morphology and the particle size of the as-prepared nanoparticles were evaluated using field emission scanning electron microscopy (FE-SEM, MIRA3 TESCAN). Energy-dispersive X-ray spectroscopy (EDX, PHENOM) was used for elemental analysis and measuring the percentage of different components of the prepared nanoparticles. A home-made photo-reactor (100 × 50 × 50 cm) equipped with UV and Vis lamps, as irradiation sources, was employed in photocatalytic reactions. A UV–Vis spectrophotometer (BioTek-Epoch, USA) was used to determine the dye concentration. A total organic carbon (TOC) analyzer model TOC-VCSH (Shimadzu, Japan) was used to determine the mineralization rate of IC dye in the degradation process.

The photocatalytic tests and analyses

The photocatalytic activity of Al-TiO₂/ZnFe₂O₄ nanocomposite was evaluated for the degradation of Indigo Carmine. For this purpose, 2.0 g L⁻¹ of the photocatalyst was added into 50 mL of Indigo Carmine dye solution with an initial concentration of 20 mg L⁻¹. To obtain a good dispersion and ensure adsorption–desorption equilibrium, the solution was stirred for 1 h in a dark position inside the photo-reactor before light irradiation. A 30 W fluorescent lamp (FSL T8/765, China) was used as an irradiation source. During the light irradiation for 120 min, an aliquot of 5 mL from the reaction suspension was sampled at 30 min intervals and centrifuged. The recovered photocatalyst was washed, dried, and reused for the next time. The concentration of Indigo Carmine in each extracted solution was evaluated by absorbance measurement at 610 nm and using the Indigo Carmine calibration curve. As shown in Fig. 1, the absorbance is decreased due to degradation of the dye. According to the results, the dye is degraded in almost two hours. In addition, a negligible decrease in the absorbance after the adsorption–desorption process at least for one hour is related to a slight adsorption of the dye on the Al-TiO₂/ZnFe₂O₄ nanocomposite in the absence of light. The photocatalytic activity was calculated by applying the following equation at room temperature:

$$\text{Degradation rate (\%)} = [(C_0 - C_t)/C_0] \times 100 \quad (1)$$

where C_0 , and C_t are the initial concentration of the Indigo Carmine solution, and its concentration after the irradiation time (t), respectively.

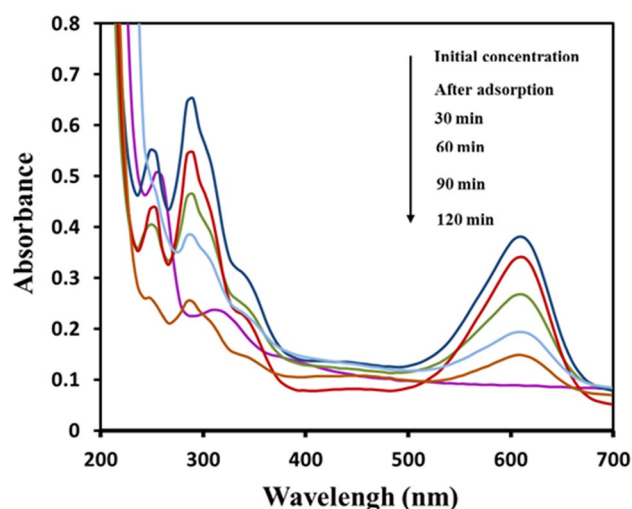


Fig. 1 UV–vis spectrum of Indigo Carmine at different intervals of the degradation process. Utilizing conditions: Photocatalyst concentration; 2 g L⁻¹, pH; 6, and Indigo Carmine concentration; 20 mg L⁻¹

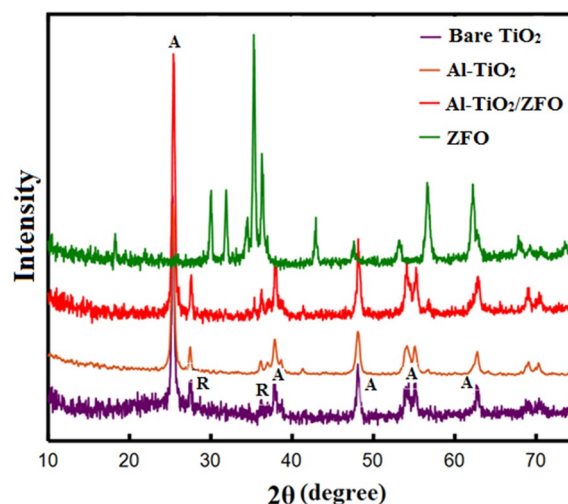


Fig. 2 XRD patterns of pure TiO₂, Al-TiO₂, Al-TiO₂/ZnFe₂O₄, and ZnFe₂O₄ nanoparticles

Results and discussion

Characterization of Al-TiO₂/ZnFe₂O₄

The XRD patterns of pure TiO₂, ZnFe₂O₄, TiO₂/ZnFe₂O₄, and Al-TiO₂/ZnFe₂O₄ nanoparticles are shown in Fig. 2. From the TiO₂ XRD pattern, it can be proved that TiO₂ consists of anatase and rutile mixtures. The peaks observed at $2\theta = 25.36^\circ$, 37.76° , 48.08° , 55.16° , 62.8° , and 69.88° belong to the anatase phase (JCPDS card No. 21–1272), and the peaks observed at around 27.26° and 36.2° belong

Table 1 The crystallite size of the synthesized samples

| Sample | ZnFe ₂ O ₄ | TiO ₂ | Al-TiO ₂ | Al-TiO ₂ /ZnFe ₂ O ₄ |
|-----------------------|----------------------------------|------------------|---------------------|---|
| Crystallite size (nm) | 25.92 | 23.54 | 23.82 | 22.35 |

to the rutile phase. The mass fraction of the anatase phase (f_A) could be calculated using Parida and Sahu's formula (Eq. 2) [35].

$$f_A = \frac{1}{1 + (I_R/0.79 I_A)} \quad (2)$$

where I_A and I_R are the intensity of the strongest diffraction line of the anatase and rutile phase, respectively. According to the diffraction peak intensities of 101 (anatase) and 110 (rutile) planes of TiO₂ that are shown in Fig. 2, the mass fraction of anatase and rutile TiO₂ in the synthesized Al-TiO₂/ZnFe₂O₄ nanocomposite was found to be 84% and 16%, respectively. The average crystallite sizes of the synthesized samples were calculated using the following Scherrer's equation.

$$D = 0.9 \lambda / \beta \cos \theta \quad (3)$$

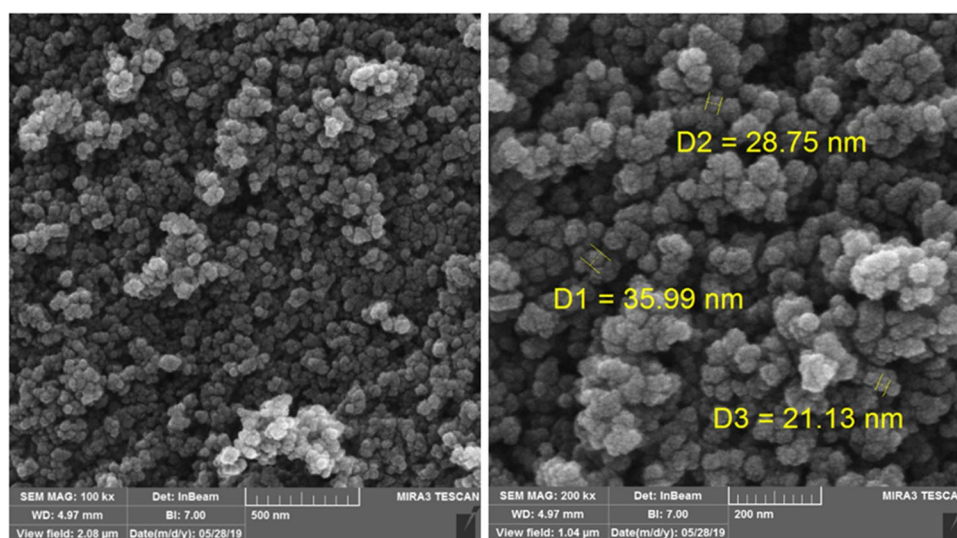
where D is the crystallite diameter (nm), λ is the wavelength of the radiation (0.15418 nm), β is the full width of the strongest peak at half height, and θ is the diffraction angle of the strongest peak. The average crystalline diameter of the synthesized samples was estimated from the diffraction peaks data at $2\theta = 25.3^\circ$ and 35.7° which correspond to (101) and (311) plane of TiO₂ and ZnFe₂O₄, respectively. The obtained results are given in Table 1. According to Fig. 2, the XRD patterns of pure TiO₂ and ZnFe₂O₄ are good agreement with the reported patterns, and there is no any peak shift in the patterns [24]. However, there is not any well-known peak that belongs to dopant in the

Al-TiO₂/ZnFe₂O₄ pattern, which is attributed to low aluminum concentration in the crystalline structure. As shown in Fig. S1, the energy-dispersive X-ray spectroscopy (EDX) study confirms the presence of Ti, O, and Al elements in the Al-doped TiO₂ nanoparticles with a mass percentage of 0.5 wt% aluminum. In the XRD pattern of ZnFe₂O₄, the peaks observed at $2\theta = 30.04^\circ$, 30.88° , 35.7° , 42.8° , 47.6° , 53.12° , 56.72° , and 62.2° , which also highly correspond with standard samples (JCPDS card No. 22–1012) proves that the nanoparticles have been synthesized favorably. In the XRD pattern of Al-TiO₂/ZnFe₂O₄ nanoparticles, the strong peaks are related to the TiO₂, and the peaks related to the ZnFe₂O₄ nanoparticles have low intensity due to the low concentration of ZnFe₂O₄ nanoparticles.

As shown in Fig. 3, field emission scanning electron microscopy analysis of the Al-TiO₂/ZnFe₂O₄ nanocomposite confirms that the nanoparticles are spherical grains with high porosity. The presence of open pores and high cavities evidence abundant surface area of the fabricated nanophotocatalyst. The FESEM-mapping of the synthesized Al-TiO₂/ZnFe₂O₄ nanocomposite (Fig. S2) shows the uniform distribution of Al, Ti, O, Zn and Fe elements in the nanocomposite structure. Moreover, the particle size distribution histogram of the nanoparticles (Fig. S3) clearly shows that the particle size is about 5 to 70 nm, and the highest plenty is related to nanoparticles of 20 nm in size.

Figure 4 shows the FT-IR spectra of pure TiO₂, Al-TiO₂, Al-TiO₂/ZnFe₂O₄ and ZnFe₂O₄ nanoparticles. The peaks in about 1600 cm^{-1} and 3400 cm^{-1} in all samples may be attributed to the hydroxyl group [36]. In all spectra of pure TiO₂, Al-TiO₂, and Al-TiO₂/ZnFe₂O₄, the broadband between 400 cm^{-1} and 1000 cm^{-1} is related to the stretching vibration of Ti–O–Ti [37]. For the zinc ferrite nanoparticles, two special peaks observed in 433.43 and 547.67 cm^{-1} are related to Zn–O and Fe–O vibrations, respectively [38, 39]. The existence of all the above-mentioned characteristic

Fig. 3 FESEM images of the Al-TiO₂/ZnFe₂O₄ nanocomposite at 100,000×m (left) and 200,000×m (right) magnifications



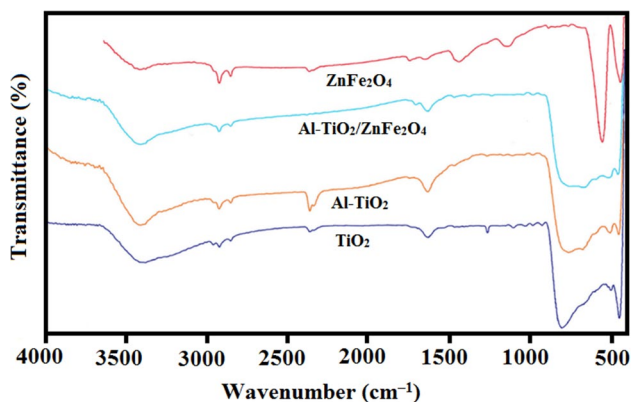
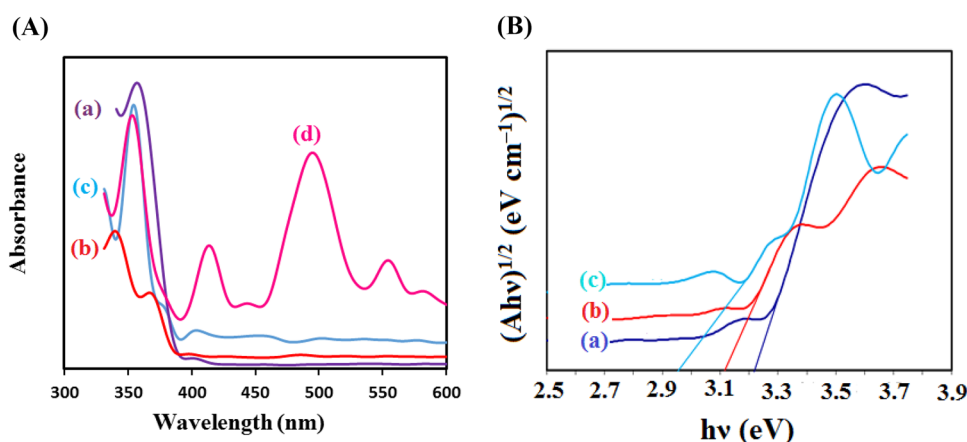


Fig. 4 FT-IR spectra of pure TiO_2 , Al-TiO_2 , ZnFe_2O_4 , and $\text{Al-TiO}_2/\text{ZnFe}_2\text{O}_4$ nanocomposite

peaks in the $\text{Al-TiO}_2/\text{ZnFe}_2\text{O}_4$ spectrum indicates the successful hybridization of Al-TiO_2 with ZnFe_2O_4 . However, the weak peaks intensity related to ZnFe_2O_4 in the $\text{Al-TiO}_2/\text{ZnFe}_2\text{O}_4$ is attributed to the low mass percentage of the ZnFe_2O_4 (5 wt%) in the final structure.

The UV–vis diffuse reflectance spectra (DRS) of bare TiO_2 , ZnFe_2O_4 , Al-doped TiO_2 , and $\text{Al-TiO}_2/\text{ZnFe}_2\text{O}_4$ nanocomposite are given in Fig. 5A. Based on the optical absorption edge obtained from the DRS spectra, the energy band gaps (E_g) for the synthesized samples were estimated using the Tauc's equation by plotting $(Ah\nu)^{1/2}$ versus to $h\nu$, where A is the absorption coefficient, and $h\nu$ is the photon energy. Based on the obtained results that are given in Fig. 5B, the bare TiO_2 and Al-TiO_2 show the absorption edges at 386 and 397 nm corresponding to band gaps of 3.21 and 3.12 eV, respectively. However, the absorption edge shifts to around 420 nm corresponding to a band gap of 2.95 eV by deposition of ZnFe_2O_4 over Al-TiO_2 . As a result, the band gap gets reduced from UV region (3.21 eV) in bare TiO_2 to visible region (2.95 eV) in the case of $\text{Al-TiO}_2/\text{ZnFe}_2\text{O}_4$ nanocomposite. Accordingly, the fabricated $\text{Al-TiO}_2/\text{ZnFe}_2\text{O}_4$

Fig. 5 (A) Diffuse reflectance spectra, and (B) Tauc's plots of (a) bare TiO_2 , (b) Al-doped TiO_2 , (c) $\text{Al-TiO}_2/\text{ZnFe}_2\text{O}_4$ nanocomposite and (d) bare ZnFe_2O_4 nanoparticles



nanocomposite shows a significant absorption in visible region and may enhance the photocatalytic degradation efficiency of IC dye under visible light irradiation.

Optimization of the photocatalytic degradation procedure

The effect of the amount of $\text{Al-TiO}_2/\text{ZnFe}_2\text{O}_4$ photocatalyst on the degradation of IC dye was inspected in the range of $0.5\text{--}3.0\text{ g L}^{-1}$ under visible light irradiation, and the results are given in Fig. 6. A noticeable enhancement in the IC degradation is observed with increasing the photocatalyst dosage from 0.5 to 2.0 g L^{-1} . However, further increase in the photocatalyst dosage from 2.0 to 3.0 g L^{-1} leads to a slight decrease in the degradation efficiency. The following factors along with the turbidity of the solution may be involved in

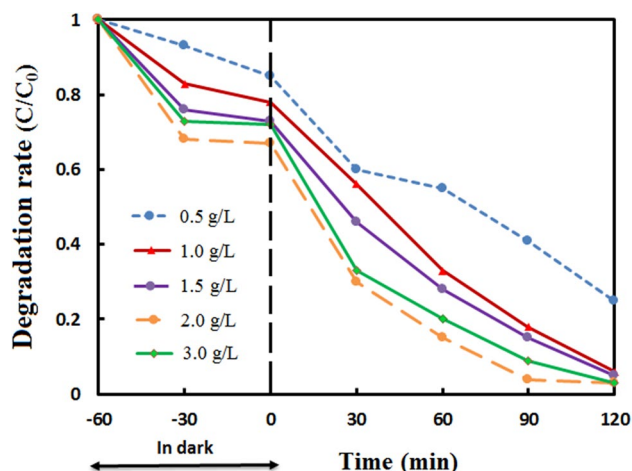


Fig. 6 Effect of $\text{Al-TiO}_2/\text{ZnFe}_2\text{O}_4$ concentration on its photocatalytic activity. Utilizing conditions: Indigo Carmine concentration; 20 mg L^{-1} , pH; 6, and visible light irradiation time; 120 min

the degradation efficiency decrease at high concentrations of Al-TiO₂/ZnFe₂O₄ [24]. (i) Owing to the nanoparticles' agglomeration at high concentrations, the total surface area of Al-TiO₂/ZnFe₂O₄ may reduce. (ii) The visible light may be blocked to some extent at high concentrations of Al-TiO₂/ZnFe₂O₄, leading to suppress the full capacity of the photocatalytic reaction. (iii) The de-activation of the active surface sites of electron and hole may occur at high concentrations of Al-TiO₂/ZnFe₂O₄ because the collision probability is increased between the nanoparticles in the solution.

Figure 7 compares the capability of the photocatalyst with different weight percentages of ZnFe₂O₄ and Al for degradation of 20 mg L⁻¹ IC dye under visible light irradiation. It is worth restating that TiO₂ is inactive under visible light owing to its vast bandgap energy. Although according to the DRS results, the bandgap energy of TiO₂ is slightly reduced by doping of Al in its structure, the degradation efficiency of IC is not adequate in the presence of Al-TiO₂ and under visible light irradiation. However, the band gap energy is shifted from 3.12 to 2.95 eV by deposition of ZnFe₂O₄ over Al-TiO₂. As a result, the best photodegradation efficiency was observed in the case of Al-TiO₂/ZnFe₂O₄ nanocomposite and under visible light irradiation. To investigate the effect of ZnFe₂O₄ concentration on the photocatalytic activity, Al-TiO₂/ZnFe₂O₄ nanocomposite with different amounts of ZnFe₂O₄ was synthesized. As shown in Fig. 7A, the photodegradation efficiency increases with increase in the ZnFe₂O₄ amount from 2 to 5 wt%.

The effect of the aluminum percentage of Al-TiO₂/ZnFe₂O₄ on the photodegradation efficiency was also optimized, and the results are depicted in Fig. 7B. As can be seen, the photodegradation efficiency increases with increase in aluminum amount from 0.2 to 0.5 wt%. Doping of the metal into the semiconductor makes a region between the metal and semiconductor known as the Schottky barrier. There is a charge separation in this region owing to the difference in the electronic structure of the semiconductor and

metal [40, 41]. So, the concentration of Al plays a significant role in the degradation efficiency of IC dye by the Al-TiO₂/ZnFe₂O₄ nanocomposite. In the presence of the Al particles, the electron density is increased on the surface of the nanoparticles, and the transfer pathway of the photo-generated electrons is also facilitated. The reactive ·O₂ could be generated via the reaction between the photo-generated electrons and the adsorbed O₂. Furthermore, the recombination of the electron–hole pairs in the Al-TiO₂/ZnFe₂O₄ nanocomposite is mostly prevented by Al particles, causing an increase in the photodegradation efficiency [24].

To study the influence of initial dye concentration on the photocatalytic activity of the Al-TiO₂/ZnFe₂O₄ nanocomposite, various concentrations (10–50 mg L⁻¹) of IC dye were evaluated. As presented in Fig. 7C, the photocatalytic activity is diminished when the initial concentration of IC dye is further increased from 10 mg L⁻¹. Because, under the constant experimental conditions, the produced electron–hole pairs on the Al-TiO₂/ZnFe₂O₄ surface are constant. As a result, the produced h⁺, ·O₂⁻ and ·OH are not sufficient for complete degradation of IC dye at high concentrations. The second probable reason is the creating of more reactive intermediates on the surface of the Al-TiO₂/ZnFe₂O₄ at high concentrations of the target. Due to covering more active sites on the surface of the Al-TiO₂/ZnFe₂O₄ by the produced intermediates, the generation of active species such as ·OH, h⁺ and ·O₂⁻ is inhibited, leading to a decrease in the photocatalytic activity [42].

Mineralization assessment

The photodegradation process may result in the formation of toxic intermediate products. To evaluate the mineralization level of IC dye using the Al-TiO₂/ZnFe₂O₄ nanocomposite subjected to visible light irradiation, TOC measurements were performed. In these experiments, the TOC removal efficiency was calculated using the following equation (Eq. 4).

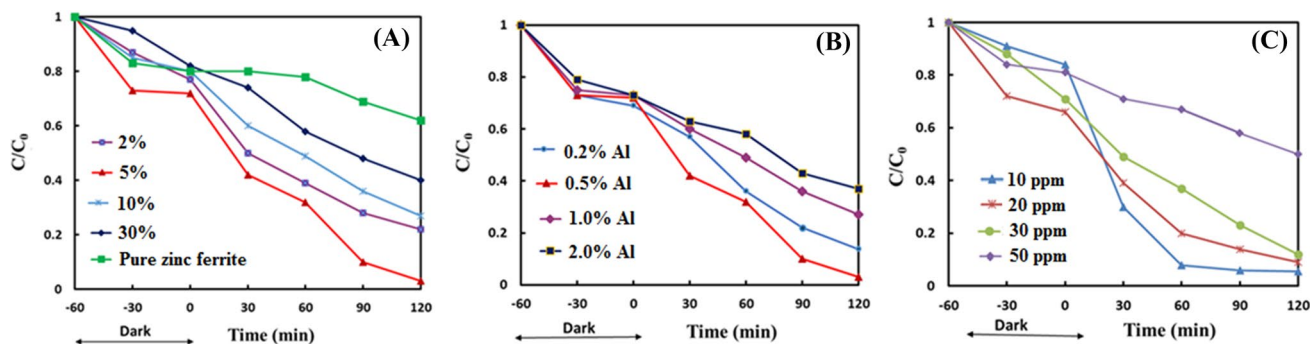


Fig. 7 Effect of different amounts (% wt) of **A** ZnFe₂O₄, **B** Al, and **C** Indigo Carmine concentration on the photocatalytic activity of Al-TiO₂/ZnFe₂O₄ nanocomposite. Utilizing conditions (**A** and **B**): Indigo

Carmine concentration; 20 mg L⁻¹, photocatalyst concentration; 2 g L⁻¹ and pH; 6, and (**C**): photocatalyst concentration; 2 g L⁻¹, pH; 6, and visible light irradiation time; 120 min

$$\text{TOC Removal (\%)} = \frac{\text{TOC}_0 - \text{TOC}_t}{\text{TOC}_0} \times 100 \quad (4)$$

where TOC_0 and TOC_t are the total organic carbon concentrations before and after a specific time of the degradation process, respectively. According to the obtained results that are shown in Fig. 8, the TOC removal efficiency increases with increase in degradation time and reaches to the maximum after 120 min of photodegradation process, indicating the fact that IC dye and its intermediates are finally converted to carbon dioxide and water in the studied photodegradation process. So, it can be concluded that photodegradation of IC dye using the $\text{Al-TiO}_2/\text{ZnFe}_2\text{O}_4$ nanocomposite under visible light irradiation leads to a significant degree of mineralization, and the presented method can be effectually used for the removal of IC dye and the byproducts from the aqueous solutions.

The kinetics of the photocatalytic degradation

The degradation of IC dye at different concentrations was further analyzed using the Langmuir–Hinshelwood model of first-order reaction kinetics according to Eq. (5) [43].

$$r = -\frac{dC}{dt} = k_r \frac{K_{ads} C}{1 + K_{ads} C} \quad (5)$$

where (r , $\text{mg L}^{-1} \text{min}^{-1}$) is the degradation rate of IC, (C , mg L^{-1}) is the concentration of IC in aqueous solution, (t , min) is the irradiation time, (k_r , min^{-1}) is the photocatalytic reaction rate constant, and (K_{ads} , Lmg^{-1}) is the adsorption coefficient of the IC onto the nano-photocatalyst. At low concentrations, $K_{ads} C$ in the denominator can be neglected,

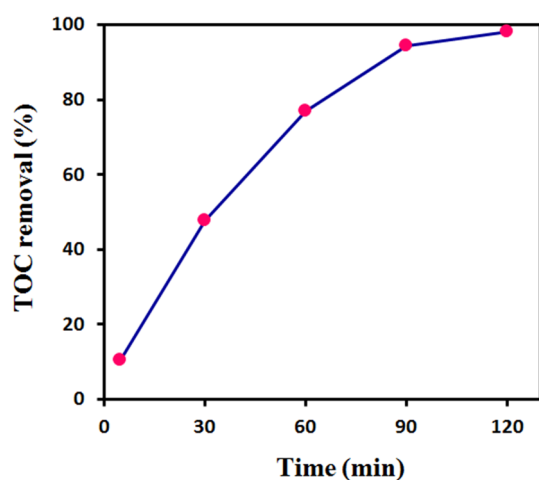


Fig. 8 The removal efficiency of TOC by $\text{Al-TiO}_2/\text{ZnFe}_2\text{O}_4$ nanocomposite under visible light irradiation. Utilizing conditions: Indigo Carmine concentration; 20 mg L^{-1} , pH; 6, and photocatalyst concentration; 2 g L^{-1}

and after integration with regard to time and concentration, Eq. 5 can be written:

$$\ln \left(\frac{C_0}{C} \right) = k_r K_{ads} t = k_{app} t \quad (6)$$

where (k_{app} , min^{-1}) is the apparent first-order photodegradation rate constant, and (C_0) and (C) are the initial and equilibrium concentration of the IC dye solution (mg L^{-1}), respectively. The IC dye photocatalytic degradation reaction with different IC concentrations ($10\text{--}50 \text{ mg L}^{-1}$), and 2 g L^{-1} $\text{Al-TiO}_2/\text{ZnFe}_2\text{O}_4$ was carried out, and variation of $\ln(C_0/C)$ versus irradiation time was constructed. As can be seen from Fig. S4, there is a linear relationship between $\ln(C_0/C)$ and irradiation time. Also, by increasing the initial concentration of IC dye from 10 to 50 mg L^{-1} , the apparent photodegradation rate constant is decreased from 0.029 to 0.0039 min^{-1} . So, the $\text{Al-TiO}_2/\text{ZnFe}_2\text{O}_4$ nanocomposite is a good catalyst for the photodegradation of IC under visible light irradiation.

Reusability and stability of the photocatalyst

The reusability and stability of the $\text{Al-TiO}_2/\text{ZnFe}_2\text{O}_4$ photocatalyst in IC dye degradation were evaluated. For this purpose, in the optimal photodegradation conditions, the prepared solution was irradiated by visible light for 120 min. Then, the photocatalyst was separated from the solution, and after washing several times with deionized water and drying at $100 \text{ }^\circ\text{C}$, the photocatalyst was reused in the degradation process. As can be seen from Fig. S5, the $\text{Al-TiO}_2/\text{ZnFe}_2\text{O}_4$ photocatalyst could be used in the IC dye degradation process for at least three continuous runs under visible light irradiation and constant experimental conditions. It is obvious that the IC dye degradation efficiency is well-preserved above 95% even after three cycles, indicating excellent stability of the photocatalyst in the degradation of IC dye.

Identification of reactive species and degradation mechanism

Analyzing of the degradation mechanism was performed by evaluation of the most active species produced during the photodegradation of IC dye. To clarify the reactive oxygen species (ROS) associate with IC dye degradation, and to suggest the photodegradation mechanism, different trapping reagents such as ethylenediaminetetraacetic acid (EDTA), isopropanol (IPA), and benzoquinone (BQ) were employed to trap the hole (h^+), hydroxyl radical (OH^\cdot), and superoxide radical (O_2^\cdot), respectively. To carry out this experiment, scavengers were added to the test solution under optimal conditions obtained from the previous steps. According to

the results that are shown in Fig. 9, although a reduction in the degradation efficiency is observed by addition of IPA and BQ in the test solution, the significant reduction in the degradation efficiency is achieved in the case of EDTA, indicating the major role of the holes (h^+) in the IC dye degradation.

Electron, hole, hydroxyl radical, and superoxide radical anions are the main species that initiate photocatalytic reactions. In the Al-TiO₂/ZnFe₂O₄ photocatalyst, ZnFe₂O₄ with a 1.92 eV bandgap initiates the photocatalytic reaction. By absorbing of light in the visible region, the electrons excite from the valence band (0.38 eV) and transfer to the conduction band on the ZnFe₂O₄ (−1.54 eV), while the holes are generated in the valence band. In the Al-TiO₂/ZnFe₂O₄ photocatalyst, the ZnFe₂O₄ as a n-type semiconductor has coupled with a p-type titanium dioxide. This combined system improves the photocatalytic efficiency by trapping, transferring, and separating the generated electron (e^-)–hole (h^+) pairs. It is worth mentioning that the ZnFe₂O₄ acts as an electrons intermediary and transfers the electrons from its lowest conduction band to the highest conduction band of the titanium dioxide. However, the photocatalytic efficiency is further improved by doping of aluminum as an electron trap in the titanium dioxide structure, which can transfer the charge to the surface and prevents electron–hole pair recombination [38, 44]. Because, Al³⁺ acts as an intermediate. It may not only accept electrons but also donates electrons so that the efficiency of the catalyst is increased by prolonging the recombination time between electrons and holes. To generate $\cdot O_2^-$, the migrated electrons further react with dissolved O₂ in the IC dye solution. On the other hand, the generated holes in the valence band of TiO₂ and ZnFe₂O₄ may directly participate in the IC dye photocatalytic degradation or react with OH[−] to generate reactive $\cdot OH$. Finally, most of the IC

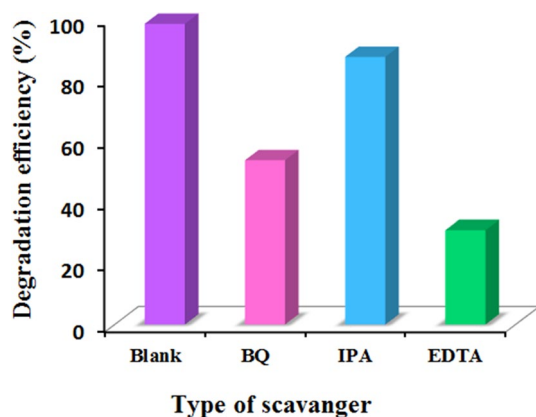
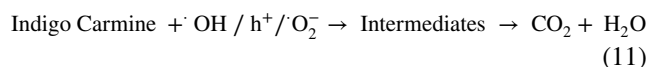
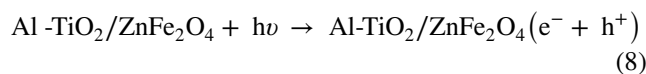
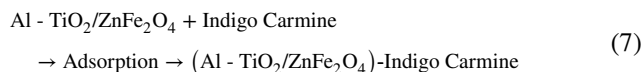


Fig. 9 Evaluation of the scavenging effect on the photocatalytic degradation of Indigo Carmine. Utilizing conditions: Indigo Carmine concentration; 20 mg L^{−1}, pH; 6, photocatalyst concentration; 2 g L^{−1}, visible light irradiation time; 120 min, and scavenger concentration; 10 mM

dye is oxidized to the end-product by $\cdot O_2^-$, $\cdot OH$, and h^+ as oxidizing agents. The photocatalytic degradation mechanism of IC dye by the Al-TiO₂/ZnFe₂O₄ nanocomposite is briefly exhibited in Fig. 10, and as follows:



Conclusions

A novel visible light-active Al-TiO₂/ZnFe₂O₄ photocatalyst was successfully prepared by a simple sol–gel method. The structural and morphological properties of the photocatalyst were well characterized by XRD, FESEM, EDX, DRS and FT-IR. The results showed that the Al-TiO₂/ZnFe₂O₄ comprised of TiO₂ and ZnFe₂O₄ nanoparticles with a particle size around 30 nm. The Al-TiO₂/ZnFe₂O₄ photocatalyst with 0.5% wt Al and 5.0% wt ZnFe₂O₄ demonstrated robust photodegradation, in which more than 98% of the target Indigo Carmine dye was removed under visible light

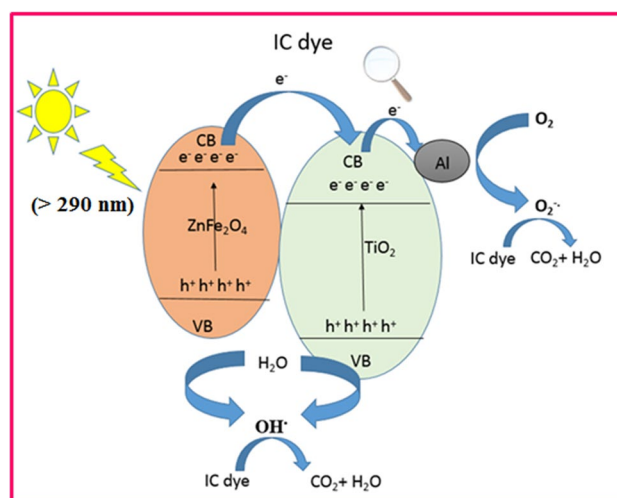


Fig. 10 Schematic representation of the proposed mechanism for Indigo Carmine photodegradation by Al-TiO₂/ZnFe₂O₄ nanocomposite

irradiation for 120 min. It was also revealed that even after three cycled usages, the Indigo Carmine degradation efficiency was maintained above 95%. The enhanced photocatalytic activity of Al-TiO₂/ZnFe₂O₄ is mainly attributed to its special heterojunction and surface structure. The improved performance of the photocatalyst is ascribed to the doped Al in the titanium dioxide structure, which acts as an electron trap for e⁻–h⁺ pair separation and prevents their recombination. The kinetics of the photocatalytic reaction was studied, and the results indicated that the photocatalytic degradation of Indigo Carmine follows pseudo-first-order degradation kinetics. A simple photocatalytic degradation mechanism, which resembles the heterostructured photocatalytic system, was also proposed.

Supplementary Information The online version contains supplementary material available at <https://doi.org/10.1007/s13738-022-02671-z>.

Acknowledgments The financial support of the research council of Azarbaijan Shahid Madani University (Grant no. ASMU/00372-21) is gratefully acknowledged.

Declarations

Conflict of interest The authors declare that they have no known competing financial interests or personal relationships that could have appeared to influence the work reported in this paper.

References

1. K.-Y. Choi, Dyes Pigm. **181**, 108570 (2020)
2. R. Yamauchi, K. Kominato, K. Mitsuyama, H. Takedatsu, S. Yoshioka, K. Kuwaki, H. Yamasaki, S. Fukunaga, A. Mori, J. Akiba, O. Tsuruta, T. Torimura, *Oncol. Lett.* **14**, 3675 (2017)
3. P.C. Genazio Pereira, R.V. Reimao, T. Pavesi, E.M. Saggiaro, J.C. Moreira, F. Veríssimo Correia, *Ecotoxicol. Environ. Saf.* **143**, 275 (2017)
4. S.Y. Janbandhu, A. Joshi, S.R. Munishwar, R.S. Gedam, *Appl. Surf. Sci.* **497**, 143758 (2019)
5. G. Sukhadeve, Shaileshkumar, Y. Janbandhu, R. Kumar, R.S. Gedam, *Chem. Select* **6**, 12873 (2021)
6. I. Othman, R.M. Mohamed, F.M. Ibrahim, *J. Photochem. Photobiol. Chem.* **189**, 80 (2007)
7. L.V.F. Oliveira, S. Bennici, L. Josien, L. Limousy, M.A. Bizeto, F.F. Camilo, *Carbohydr. Polym.* **230**, 115621 (2020)
8. M.A. Ahmed, A.A. Brick, A.A. Mohamed, *Chemosphere* **174**, 280 (2017)
9. C.M. Kalyana, K. Ramakrishna, P.V. Subba Rao, *Int. J. Chem. Sci.* **15**, 220 (2017)
10. R.O. Ramos, M.V.C. Albuquerque, W.S. Lopes, J.T. Sousa, V.D. Leite, *J. Water Proc. Eng.* **37**, 101535 (2020)
11. R. Oriol, I. Sires, E. Brillas, A.R.D. Andrade, *J. Electroanal. Chem.* **847**, 113088 (2019)
12. S.N. Ahmed, W. Haider, *Nanotechnology* **29**, 342001 (2018)
13. J. Wade, An investigation of TiO₂-ZnFe₂O₄ nanocomposites for visible light. A, College of Engineering University of South Florida, (2005)
14. S. Anandan, V. Kumar Ponnusamy, M. Ashokkumar, *Ultrason. Sonochem.* **67**, 105130 (2020)
15. D. Zhu, Q. Zhou, *Environ. Nanotechnol. Monit. Manag.* **12**, 100255 (2019)
16. J. Al-Musawi, G.O. McKay, P. Rajiv, N. Mengelizadeh, D. Balarak, *J. Photochem. Photobiol. A: Chem.* **424**, 113617 (2022)
17. M. Yilmaz, N. Mengelizadeh, M. Khodadadi Saloot, S. Shahbaksh, D. Balarak, *Mater. Sci. Semicond. Process* **144**, 106593 (2022)
18. T.J. Al-Musawi, N. Mengelizadeh, M. Taghavi, Z. Shehu, D. Balarak, *Environ. Sci. Pollut. Res.* (2022). <https://doi.org/10.1007/s11356-022-19460-z>
19. R. Saravanan, F. Gracia, A. Stephen, Basic principles, mechanism, and challenges of photocatalysis, in: *Nanocomposites for Visible Light-induced Photocatalysis*, Chapter 2, pp. 19–40, Springer (2017).
20. B. Ibrahim, ss Photocatalytic oxidation of NO_x over TiO₂ containing cement based materials, (Doctoral dissertation, MS Thesis, Middle East Technical University, Ankara, Turkey), (2013)
21. G.K. Sukhadeve, S.Y. Janbandhu, S. Upadhyay, R.S. Gedam, *J. Australian Ceram. Soc.* **58**, 39 (2022)
22. J. Wang, J. Zhao, Lu. Sun, X. Wang, *Text. Res. J.* **85**, 1104 (2015)
23. C. Byrne, G. Subramanian, S.C. Pillai, *J. Environ. Chem. Eng.* **6**, 3531 (2018)
24. Y. Jia, J. Liub, S. Chac, S. Choic, Y. Chang Parkd, C. Liua, *J. Ind. Eng. Chem.* **47**, 303 (2017)
25. M.J. Valero-Romero, J.G. Santaclara, L. Oar-Arteta, L. van Koppen, D.Y. Osadchii, J. Gascon, F. Kapteijn, *Chem. Eng. J.* **360**, 75 (2019)
26. J. Zhu, W. Mu, L. Su, X. Li, Y. Guo, S. Zhang, Z. Li, *J. Solid State Chem.* **248**, 142 (2017)
27. M.R. Delsouz Khaki, M.S. Shafeeyan, A.A. Abdul Raman, W.M. Daud, *J. Mol. Liq.* **258**, 354 (2018)
28. M.Y. Xie, K.Y. Su, X.Y. Peng, R.J. Wu, M. Chavali, W. Chen Chang, *J. Taiwan Inst. Chem. Eng.* **70**, 161 (2017)
29. A. Garg, A. Singh, V.K. Sangal, P.K. Bajpai, N. Garg, *New J. Chem.* **41**, 9931 (2017)
30. T.B. Nguyen, C. Huang, R. Doong, *Sci. Total Environ.* **646**, 745 (2019)
31. X. Meng, Y. Zhuang, H. Tang, C. Lu, *J. Alloys Compd.* **761**, 15 (2018)
32. M. Amir, H. Gungunes, A. Baykal, M.A. Almessiere, H. Sözeri, I. Ercan, M. Sertkol, S. Asiri, A. Manikandan, *J. Supercond. Nov. Magn.* **31**, 3347 (2018)
33. B. Zhang, J. Zhang, F. Chen, *Res. Chem. Intermed.* **34**, 375 (2008)
34. K. Nemade, R. Barde, S. Waghuley, *J. Taibah Univ. Sci.* **10**, 345 (2016)
35. Y. Song, Y. Kim, H. Lee, D. Yong Lee, M. Lee, B. Kim, *J. Korean Phys. Soc.* **72**, 412 (2018)
36. J. Yu, X. Zhao, J.C. Yu, *J. Mater. Sci. Lett.* **20**, 1745 (2001)
37. R. Chalasani, S. Vasudevan, *ACS Nano* **7**, 4093 (2013)
38. K. Lee, X. Chuah, Y. Cheng, S. Lu, *J. Mater. Chem. A* **3**, 18578 (2015)
39. C. Caia, Z. Zhang, J. NiShan, H. Zhang, D.D. Dionysio, *Appl. Catal. B* **182**, 456 (2016)
40. W. Wang, J. Chen, W. Li, D. Pei, X. Zhang, H. Yu, *A.C.S. Appl. Mater. Interfaces* **7**, 20349 (2015)
41. D. Ding, K. Liu, S. He, C. Gao, Y. Yin, *Nano Lett.* **14**, 6731 (2014)
42. Y. Yao, F. Lu, H. Chen, F. Wei, X. Liu, C. Lian, S. Wang, *J. Hazard. Mater.* **297**, 224 (2015)
43. R.K. Wahi, W.W. Yu, Y. Liu, M.L. Mejia, J.C. Falkner, W. Nolte, V.L. Colvin, *J. Mol. Catal. A Chem.* **242**, 48 (2005)
44. R. Amrollahi, M.S. Hamdy, G. Mul, *J. Catal.* **319**, 194 (2014)

Springer Nature or its licensor holds exclusive rights to this article under a publishing agreement with the author(s) or other rightsholder(s); author self-archiving of the accepted manuscript version of this article is solely governed by the terms of such publishing agreement and applicable law.